

Mechanical and Tribological Properties of Layered Materials Under High Pressure: Assessing the Importance of Many-Body Dispersion Effects

Supporting Information

Wengen Ouyang,¹ Ido Azuri,² Davide Mandelli,³ Alexandre Tkatchenko,⁴ Leeor Kronik,²

Michael Urbakh,¹ and Oded Hod¹

¹*School of Chemistry and The Sackler Center for Computational Molecular and Materials Science, Tel Aviv University, Tel Aviv 6997801, Israel*

²*Department of Materials and Interfaces, Weizmann Institute of Science, Rehovoth 76100, Israel*

³*Istituto Italiano di Tecnologia, Via Morego, 30, 16163 Genova, Italy*

⁴*Department of Physics and Materials Science, University of Luxembourg, L-1511 Luxembourg, Luxembourg*

This supporting information document includes the following sections:

1. Interlayer potential (ILP) fitting parameters.
2. Sensitivity test of the ILP parameters.
3. Bulk modulus of graphite and hexagonal boron nitride.
4. Sliding potential energy surfaces for bilayer configurations at sub-equilibrium interlayer distances.
5. Dispersive component of the sliding energy surfaces.
6. Sliding energy barriers under different normal loads.

1. Interlayer potential (ILP) fitting parameters

In this work, all reference data were obtained using dispersion-augmented density functional theory (DFT) calculations, which are based on the screened-exchange hybrid functional of Heyd, Scuseria, and Ernzerhof (HSE).¹⁻⁴ We employ both many-body dispersion (MBD)^{5, 6} and Tkatchenko-Scheffler (TS) corrections^{7, 8} to augment the HSE functional. In previous studies, the former scheme (HSE + MBD) was shown to provide a good balance between accuracy and computational burden for calculating binding energy curves and sliding energy landscapes for bilayer graphene, *h*-BN, and their heterojunctions.^{9, 10} In recent work, we refined the ILP parameters to fit against the MBD corrected DFT reference for bilayer systems and improved the performance of the potential at the sub-equilibrium regime.¹¹ In the present study, to evaluate the properties of bulk materials, we performed DFT calculations for a fully periodic system (bulk configuration) with the same method. The resulting binding energy curves and sliding energy surfaces appear in Figures 1-3 of the main text. By using the fitting procedure introduced in ref [11](#), two sets of parameters, fitted against the HSE + MBD and HSE + TS DFT reference data, are given in **Table S1** and **Table S2**.

Table S1. List of ILP parameter values for bulk graphene and bulk h-BN based systems that are periodic in all directions. The training set includes all HSE + MBD binding energy curves and sliding potential surfaces appearing in Figs. 1-3 of the main text. A value of $R_{cut} = 16 \text{ \AA}$ is used throughout.

	$\beta_{ij} (\text{\AA})$	α_{ij}	$\gamma_{ij} (\text{\AA})$	$\varepsilon_{ij} (\text{meV})$	$C_{ij} (\text{meV})$	d_{ij}	$s_{R,ij}$	$r_{eff,ij} (\text{\AA})$	$C_{6,ij} (\text{eV}\cdot\text{\AA}^6)$	$\lambda_{ij} (\text{\AA}^{-1})$
C-C	3.1894	8.2113	1.2600	0.0106	38.9821	10.9736	0.7869	3.4579	25.2496	--
B-B	3.2147	7.1652	1.7459	11.0736	15.4819	15.4815	0.8550	3.4424	49.4984	0.70
N-N	3.3006	6.9226	1.4845	7.9908	46.6115	16.9081	0.7585	3.3266	14.8106	0.69
B-N	3.1709	8.5168	2.8657	5.4561	2.5548	13.5321	0.8863	3.4553	24.6708	0.694982
C-B	3.1007	5.1146	3.8387	18.2345	1.1902	10.2155	0.7686	3.5030	39.2629	--
C-N	3.3173	10.3497	1.3793	16.3163	19.5691	15.7748	0.5645	3.2659	19.9631	--

Table S2. List of ILP parameter values for bulk graphene and bulk h-BN based systems that are periodic in all directions. The training set includes all HSE + TS binding energy curves and sliding potential surfaces appearing in Figs. 1-3 of the main text. A value of $R_{cut} = 16 \text{ \AA}$ is used throughout.

	$\beta_{ij} (\text{\AA})$	α_{ij}	$\gamma_{ij} (\text{\AA})$	$\varepsilon_{ij} (\text{meV})$	$C_{ij} (\text{meV})$	d_{ij}	$s_{R,ij}$	$r_{eff,ij} (\text{\AA})$	$C_{6,ij} (\text{eV}\cdot\text{\AA}^6)$	$\lambda_{ij} (\text{\AA}^{-1})$
C-C	3.1912	8.8423	1.1312	0.0863	33.4354	10.0196	0.9251	3.4842	32.4025	--
B-B	3.5386	5.1268	2.2006	12.8753	27.5894	13.3600	0.8414	3.6431	99.5133	0.70
N-N	3.5915	3.2218	1.4354	6.6766	73.1026	13.0710	0.7466	3.3083	74.8236	0.69
B-N	3.9929	7.8553	2.5853	4.5785	2.3284	16.2665	0.8669	3.9824	84.7000	0.694982
C-B	3.0183	9.8126	3.6974	22.1591	0.8265	11.1783	0.9510	3.8465	40.1653	--
C-N	3.4896	10.1614	1.1615	4.2615	11.1811	11.0391	0.9257	3.2512	29.0669	--

2. Sensitivity test of the ILP parameters

In this section we investigate in some details the effects of the choice of the reference datasets (HSE + TS and HSE + MBD) on the ILP parametrization. For the sake of the discussion, we report here the analytical expression of the ILP:

$$V(r_{ij}, n_i, n_j) = \text{Tap}(r_{ij})[V_{\text{att}}(r_{ij}) + V_{\text{rep}}(r_{ij}, n_i, n_j) + V_{\text{Coul}}(r_{ij})],$$

where

$$\text{Tap}(r_{ij}) = 20 \left(\frac{r_{ij}}{R_{\text{cut}}} \right)^7 - 70 \left(\frac{r_{ij}}{R_{\text{cut}}} \right)^6 + 84 \left(\frac{r_{ij}}{R_{\text{cut}}} \right)^5 - 35 \left(\frac{r_{ij}}{R_{\text{cut}}} \right)^4 + 1$$

provides a continuous long-range cutoff (up to third derivative) that dampens the various interactions at interatomic separations larger than $R_{\text{cut}} = 16 \text{ \AA}$, and

$$V_{\text{Coul}}(r_{ij}) = kq_i q_j / \sqrt[3]{r_{ij}^3 + \lambda_{ij}^{-3}}$$

is the monopolar electrostatic interaction between atoms i and j . We note that the parameters, λ_{ij} , and the atomic charges, q_i , are the same for both the HSE + TS and HSE + MBD parametrizations. Hence, to understand the effects of the chosen model on the ILP, we can consider only the terms V_{att} and V_{rep} , corresponding to the long-range van der Waals attraction and short-range Pauli repulsion, respectively:

$$V_{\text{att}}(r_{ij}) = - \frac{1}{1 + e^{-d_{ij}[r_{ij}/(s_{R,ij} r_{ij}^{\text{eff}}) - 1]}} \frac{C_{6,ij}}{r_{ij}^6}$$

$$V_{\text{rep}}(r_{ij}, n_i, n_j) = e^{\alpha_{ij} \left(1 - \frac{r_{ij}}{\beta_{ij}} \right)} \left\{ \varepsilon_{ij} + C_{ij} \left[e^{-(\rho_{ij}/\gamma_{ij})^2} + e^{-(\rho_{ji}/\gamma_{ij})^2} \right] \right\}$$

Here, r_{ij} is the Euclidean distance between the two atoms involved, n_i is the surface normal at the position of atom i and ρ_{ij} is the lateral distance between the normal vectors at the positions of atoms i and j .

To study the effects of the chosen model on the ILP, in the first row of **Figure S1** we compare the ILP-TS-bulk and ILP-MBD-bulk binding energy curves computed for three periodic systems: graphite, bulk h -BN and alternating graphene/ h -BN. For all cases considered, the minimum of the ILP-TS-bulk curve (dashed blue lines in **Figure S1**) is $\lesssim 50$ meV/atom lower than the value predicted by the ILP-MBD-bulk parametrization (continuous red lines). This is accompanied by only minor changes in the equilibrium interlayer distance (differences $\lesssim 3\%$, as reported also in Table 1 and Table 2 of the main text). Differences between the HSE + TS and HSE + MBD parameterized ILP curves become negligible at interlayer distances $d \gtrsim 6 \text{ \AA}$.

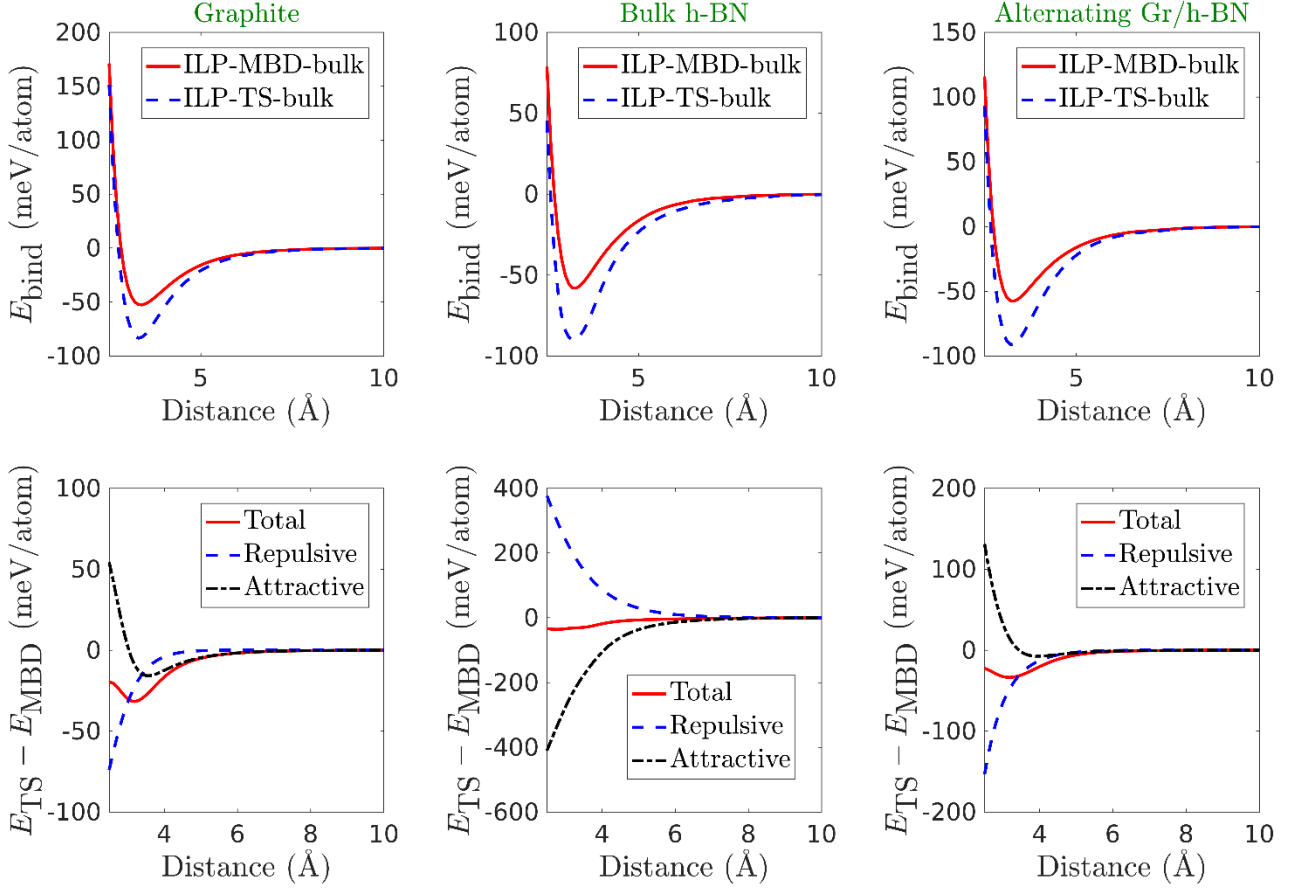


Figure S1. Comparison between HSE + TS and HSE + MBD parametrized ILP binding energy curves for graphite (left column), bulk h-BN (middle column), and bulk alternating graphene/h-BN. The first row reports the comparison between the binding energy curve corresponding to the MBD (solid red line) and TS (blue dashed line) parametrization of the ILP, for three systems: graphite (left panel), bulk h-BN (middle panel), and alternating graphene/h-BN (right panel). The second row reports the corresponding differences between the ILP-TS-bulk and ILP-MBD-bulk binding energy curves (solid red lines), between the MBD and TS Pauli repulsion components (blue dashed line) and between the ILP-MBD-bulk and ILP-TS-bulk van der Waals attractive components (dotted-dash black line).

To better understand the origin of the observed variations, in the second row of **Figure S1** we report the difference between the ILP-MBD-bulk and ILP-TS-bulk binding energy curves (red continuous lines), together with the difference computed considering only the repulsive (dashed blue lines) or the attractive (dash-dotted black lines) terms. For the case of graphite, the TS parametrization predicts larger attraction at interlayer distances $d \lesssim 3 \text{ \AA}$, which becomes smaller than the MBD prediction between $3 \lesssim d \lesssim 6 \text{ \AA}$. A detailed analysis of the effects of each single parameter on the ILP reveals that these two outcomes are due to the changes of the $C_{6,ij}$ and $s_{R,ij}$ parameters, respectively (see first row of **Table S3**, and last row of **Figure S2**). The Pauli repulsion predicted by the TS parametrization is instead always smaller than the one predicted the MBD parametrization. This is mainly caused by the variation of the C_{ij} and γ_{ij} parameters (see first two

rows of **Figure S2**). For the case of bulk h-BN (middle panels in **Figure S1**), the repulsive and attractive parts computed via the TS parametrization are respectively larger and smaller than the corresponding MBD values. The origin of these differences are mainly due to the changes of the β_{ij} , C_{ij} , and α_{ij} parameters for the repulsive part, and to the changes of the $C_{6,ij}$ parameter for the attractive part (see **Table S3** and **Figure S3**). Finally, for the case of the alternating graphene/h-BN system, we observe an opposite behavior, where the repulsive and attractive interactions predicted by the TS parametrization are respectively smaller and larger than the corresponding MBD values (see bottom right panel in **Figure S1**). The detailed analysis reported in **Figure S4** demonstrates that this behavior arises from the interplay of several parameters.

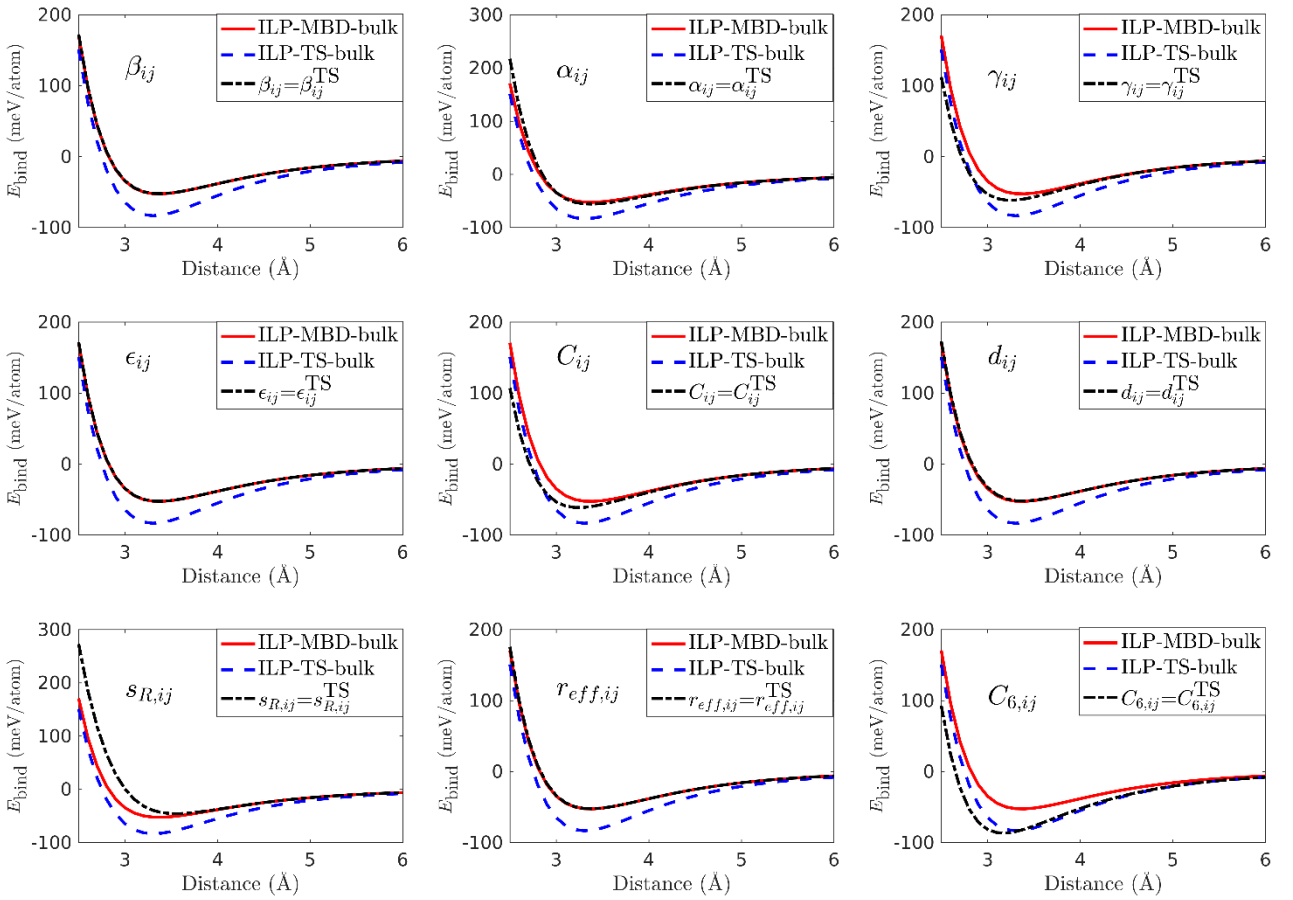


Figure S2. Sensitivity of the ILP to changes in parameter values for bulk graphite. In each panel, the red solid line and blue dashed line are binding energy curves computed using the MBD and TS parameterizations, respectively. The black dash-dotted line is the binding energy curve calculated using the MBD values for all parameters except one (labeled in each panel), which is changed to the corresponding TS values, for each distinct pair of atoms, as reported in **Table S3**.

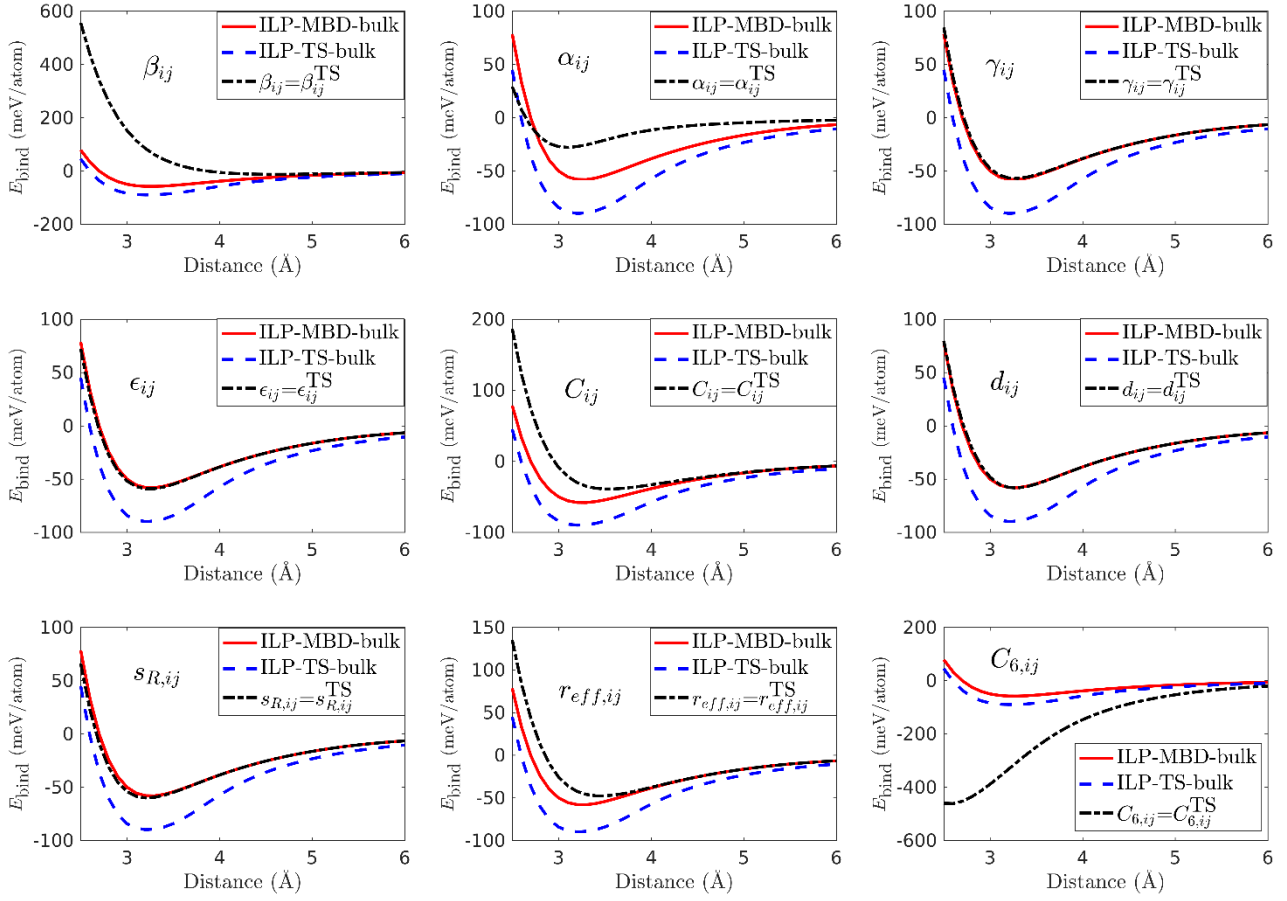


Figure S3. Sensitivity of the ILP to changes in the parameter values for bulk h-BN. In each panel, the red solid line and blue dashed line are binding energy curves computed using the MBD and TS parameterizations, respectively. The black dash-dotted line is the binding energy curve calculated using the MBD values for all parameters except one (labeled in each panel), which is changed to the corresponding TS values, for each distinct pair of atoms, as reported in **Table S3**.

Table S3. For each pair of atom, we report the change, $\Delta X = (X_{TS} - X_{MBD})/X_{MBD}$, of the various ILP parameters obtained from the HSE + TS parametrization, relative to the value obtained from the HSE + MBD parametrization.

	$\Delta\beta_{ij}$ (%)	$\Delta\alpha_{ij}$ (%)	$\Delta\gamma_{ij}$ (%)	$\Delta\epsilon_{ij}$ (%)	ΔC_{ij} (%)	Δd_{ij} (%)	$\Delta s_{R,ij}$ (%)	$\Delta r_{eff,ij}$ (%)	$\Delta C_{6,ij}$ (%)	$\Delta\lambda_{ij}$ (%)
C-C	0.06	7.7	-10	714	-14	-8.8	18	0.76	28	--
B-B	10.0	-28	26	16	78	-14	-1.6	5.8	101	0
N-N	8.8	-53	-3.3	-16	57	-23	-1.6	-0.55	405	0
B-N	26	-7.8	-9.8	-16	-8.9	20	-2.2	15	243	0
C-B	-2.7	92	-3.7	22	-31	9.4	24	9.8	2.3	--
C-N	5.2	-1.8	-16	-74	-43	-30	64	-0.45	46	--

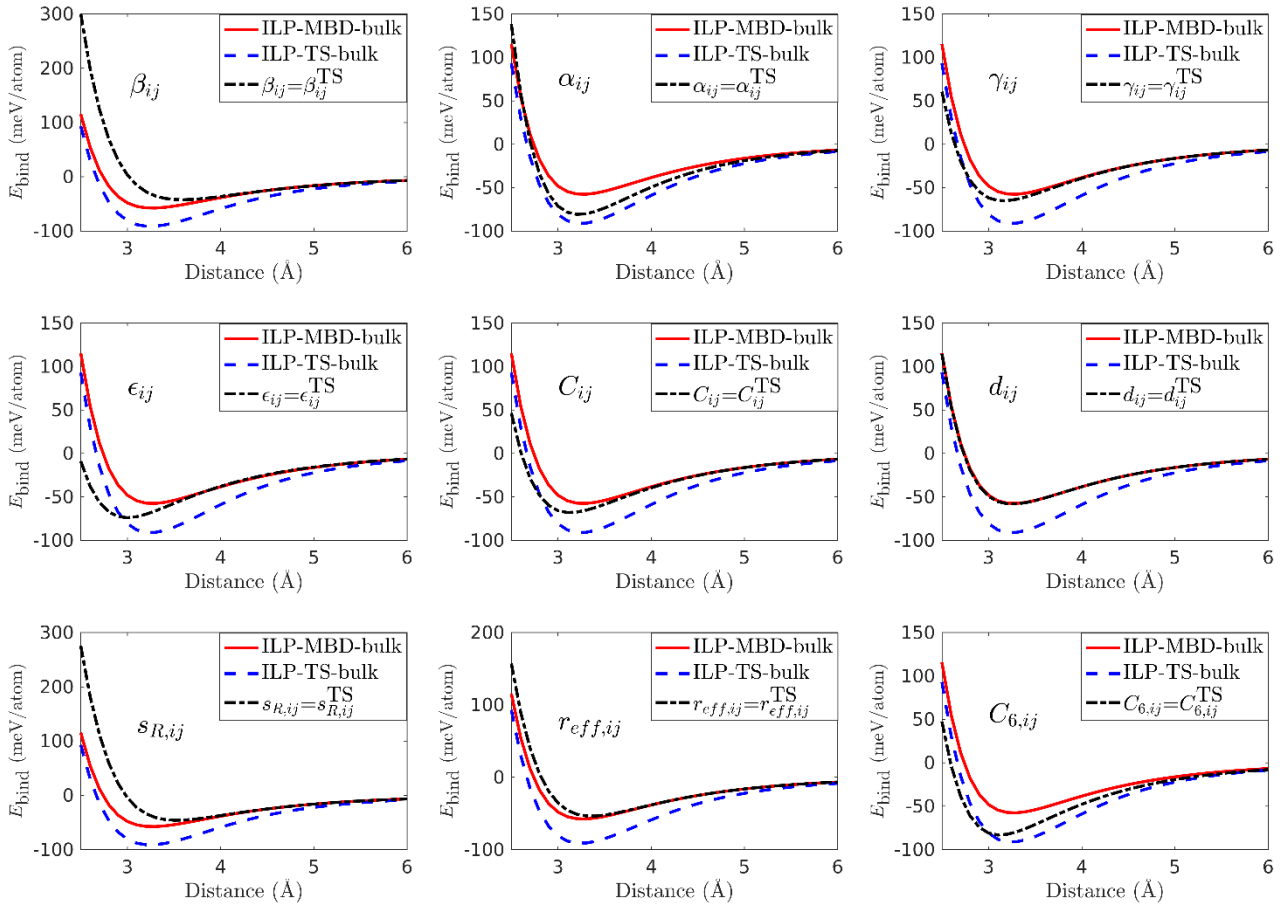


Figure S4. Sensitivity of the ILP to changes in parameter values for bulk alternating graphene/h-BN configuration. In each panel, the red solid line and blue dashed line are binding energy curves computed using the MBD and TS parameterizations, respectively. The black dash-dotted line is the binding energy curve calculated using the MBD values for all parameters except one (labeled in each panel), which is changed to the corresponding TS values, for each distinct pair of atoms, as reported in **Table S3**.

Overall, the above analysis that focused on binding energy curves suggests that changing the reference model affects different parameters in different ways, depending on the material considered. The combined effects of such changes on the ILP determines the final shape of the binding energy curves. This, of course, is a general feature of force-field parameterizations. While all parameter values are kept within reasonable physical ranges during the optimization procedure, discussing separately the specific value of each parameter goes beyond the accuracy limits of the method and only their combined behavior should be considered. Nevertheless, from a careful inspection of **Figure S2-Figure S4** it becomes clearly evident that the binding energy curve can be very sensitive to the value of some parameters, especially the isotropic long-range attraction $C_{6,ij}$ coefficients and the anisotropic repulsion C_{ij} coefficients. Therefore, extra care should be taken when fitting their values.

3. Bulk modulus of graphite and hexagonal boron nitride

Figure S5 shows the normalized volume V/V_0 (V_0 being the volume at zero pressure) of bulk graphite and bulk h -BN, as a function of pressure. The open symbols represent equilibrium molecular dynamics (EMD) simulation results obtained with different ILP and Kolmogorov-Crespi (KC) potential parameterizations.⁹⁻¹² The solid lines are the fitted Murnaghan equation (eq 1 in the main text) results.¹³ The fitted parameters (bulk modulus and its pressure derivative) are listed in Tables 1-2 in the main text for bulk graphite and bulk h -BN, respectively.

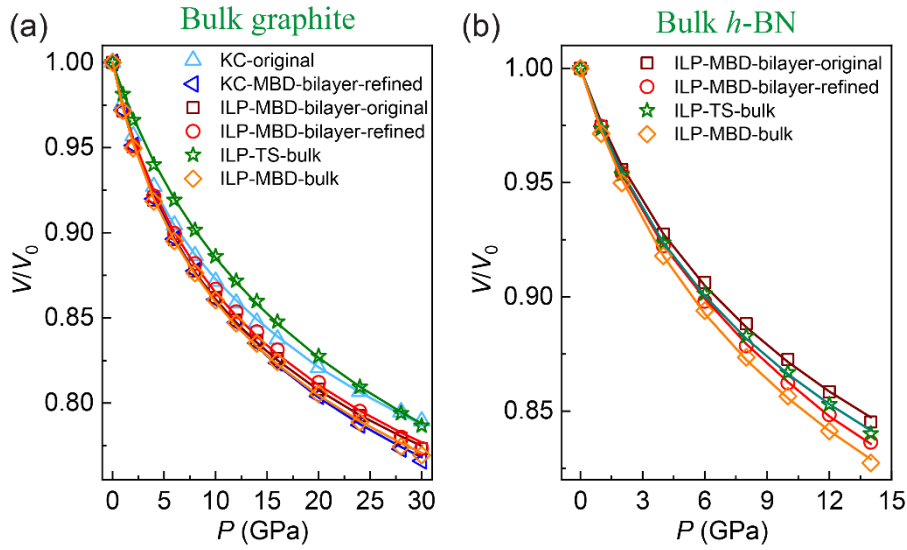


Figure S5. Pressure dependence of the normalized volume V/V_0 of bulk graphite and bulk h -BN. The open points are the NPT simulation results for different parameterizations of the ILP and KC potentials. The solid lines are fitted curves generated by eq 1 in the main text.

It should be noted that apart from the Murnaghan equation, two other equations of state (EOS) are also commonly used to fit the P - V curve: (i) The Birch-Murnaghan equation (eq S1)^{14,15} and (ii) The Vinet equation (eq S2),^{16,17} which take the following forms:

$$P = 3B_V^0 \xi (1 + 2\xi)^{5/2} \left[1 - \frac{3}{2} (4 - B_V') \xi \right], \quad \xi = \frac{1}{2} \left[\left(\frac{V}{V_0} \right)^{-2/3} - 1 \right], \quad (\text{S1})$$

$$P = 3B_V^0 \frac{(1-X)}{X^2} \exp \left[\frac{3}{2} (B_V' - 1)(1 - X) \right], \quad X = \left(\frac{V}{V_0} \right)^{1/3}. \quad (\text{S2})$$

As in the Murnaghan equation, these two EOS also assume that B_V varies with pressure (hence the inclusion of B_V'). Nonetheless, they differ in their description of the dependence of B_V on the pressure, by assuming that it is linear, polynomial, and exponential for the Murnaghan, Birch-Murnaghan, and Vinet EOS, respectively.

Table S4 lists the fitting EMD results for the bulk modulus of graphite and bulk *h*-BN with the three commonly used EOS. Unlike the observations from a previous study,¹⁸ where the bulk modulus was found to be very sensitive to the choice of EOS, here we find that all three EOS yield comparable values for the bulk modulus. This suggests that the differences between the experimental values of the bulk modulus arise from the different measuring techniques adopted in different studies rather than from the choice of the EOS used for the fitting procedure.

Table S4. Bulk moduli obtained by fitting our EMD data with different equations of state for graphite and bulk *h*-BN. Experimental values are presented for comparison.

Material	Methods	Murnaghan		Birch-Murnaghan		Vinet	
		B_V^0 (GPa)	B_V'	B_V^0 (GPa)	B_V'	B_V^0 (GPa)	B_V'
Graphite	Experiments	33±2 ^a	12.3±0.7 ^a	--	--	--	--
		33.8±0.3 ^b	8.9±0.1 ^b	--	--	--	--
		--	--	--	--	30.8±2 ^c	--
	ILP-MBD-bulk	34±1	8.1±0.3	27±1	14.2±0.7	31.5±0.8	10.2±0.2
	ILP-TS-bulk	55±2	6.2±0.3	53±0.9	7.5±0.2	53.4±0.9	7.4±0.2
	ILP-MBD-bilayer-refined, ref 11	36±3	8.1±0.6	33±2	12.2±0.9	36±2	9.6±0.5
	ILP-MBD-bilayer-original, ref 10	33±1	8.5±0.3	25.5±0.8	16.3±0.7	30.7±0.3	10.8±0.1
	KC-MBD-bilayer-refined, ref 11	35±2	7.7±0.3	30.5±0.5	12.0±0.3	33.5±0.7	9.5±0.2
	KC-original, ref 12	37±2	8.9±0.4	29.3±0.6	16.7±0.4	35.1±0.7	11.1±0.2
Bulk <i>h</i> -BN	Experiments	22±4 ^a	18±3 ^a	--	--	--	--
		36.7±0.5 ^d	5.6±0.2 ^d	--	--	--	--
		--	--	17.6±0.8 ^e	19.5±3.4 ^e	--	--
		--	--	27.6±0.5 ^f	10.5±0.5 ^f	--	--
	ILP-MBD-bulk	33±2	7.8±0.6	31±1	10.2±0.8	32±1	9.0±0.5
	ILP-TS-bulk	35±2	8.7±0.6	33±1	12.0±0.7	34±1	10.0±0.5
	ILP-MBD-bilayer-refined, ref 11	35±2	8.0±0.6	33±1	10.5±0.7	34±1	9.2±0.5
	ILP-MBD-bilayer-original, ref 10	38±3	8.7±0.9	36±2	11±1	38±2	9.7±0.9

^aref [19](#), ^bref [20](#), ^cref [21](#), ^dref [22](#), ^eref [23](#), ^fref [24](#).

4. Sliding potential energy surfaces for bilayer configurations at sub-equilibrium interlayer distances

Because the repulsive walls of the binding energy curves are very steep at the sub-equilibrium interlayer distance regime, the differences between energy and forces calculated using different methods are expected to increase in absolute value in this range. To demonstrate this, we present in **Figure S6-Figure S8** the sliding potential energy surfaces for periodic bilayer graphene and bilayer *h*-BN, calculated using the refined ILP and KC potential¹¹ as well as the original ILP¹⁰ and KC potentials,¹² at three sub-equilibrium interlayer distances. The first and second rows in **Figure S6** present the sliding energy surfaces of periodic bilayer graphene with interlayer distances of 3.35 Å (left column), 3.0 Å (middle column) and 2.8 Å (right column), calculated using the refined¹¹ and original ILP,¹⁰ respectively. The differences between the two are presented in the third row of the figure. Clearly, the differences between the sliding energy surfaces obtained using the two parameterizations increase in both magnitude and relative value as the interlayer distance decreases. Specifically, the maximal absolute differences obtained are 0.4 (~2%), 2 (~13%), and 8 meV/atom (~20%) for interlayer distances of 3.35 Å, 3.0 Å, and 2.8 Å, respectively.

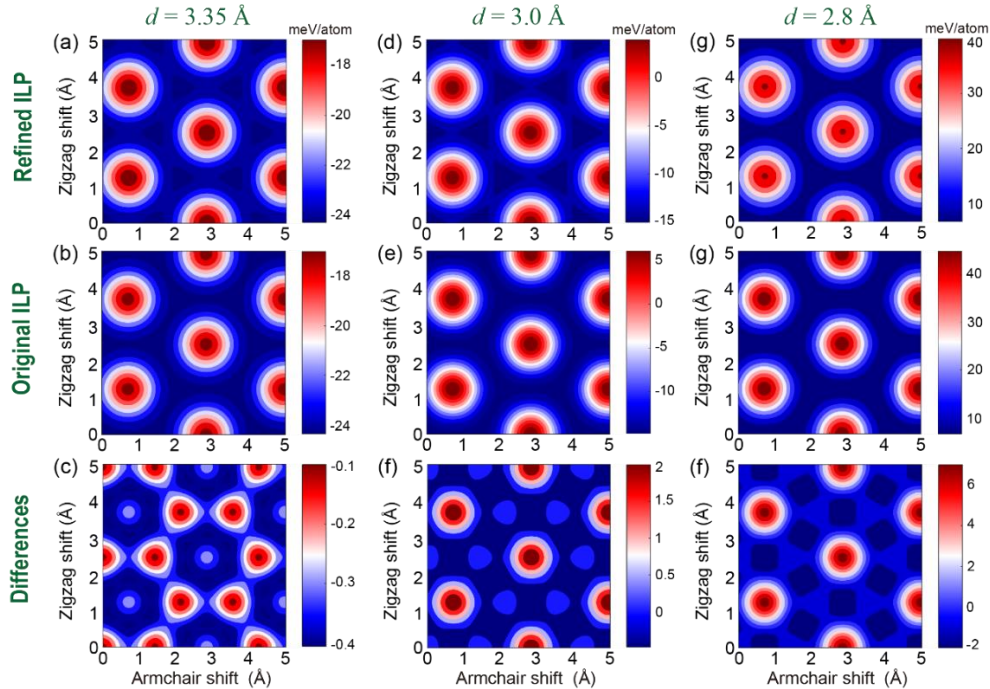


Figure S6. Sliding energy surfaces of periodic bilayer graphene for three different interlayer distances. The first and second rows present the sliding energy surfaces obtained at interlayer distances of 3.35 Å (left column), 3.0 Å (middle column), and 2.8 Å (right column) calculated using the refined¹¹ and original graphene ILP,¹⁰ respectively. The third row presents the differences between the results obtained using the two ILP parameterizations.

The first and second rows in **Figure S7** present the sliding energy surfaces of periodic bilayer graphene with interlayer distances of 3.35 Å (left column), 3.0 Å (middle column) and 2.8 Å (right column) calculated using the refined and original KC potential, respectively. The differences between the two are presented in the third row of the figure. Clearly, the differences between the sliding energy surfaces obtained using the two parameterizations increase in both magnitude and relative value as the interlayer distance decreases. Specifically, the maximal absolute differences obtained are 2.2 (~10%), 5.3 (~20%), and 16.4 meV/atom (~40%), for interlayer distances of 3.35 Å, 3.0 Å, and 2.8 Å, respectively.

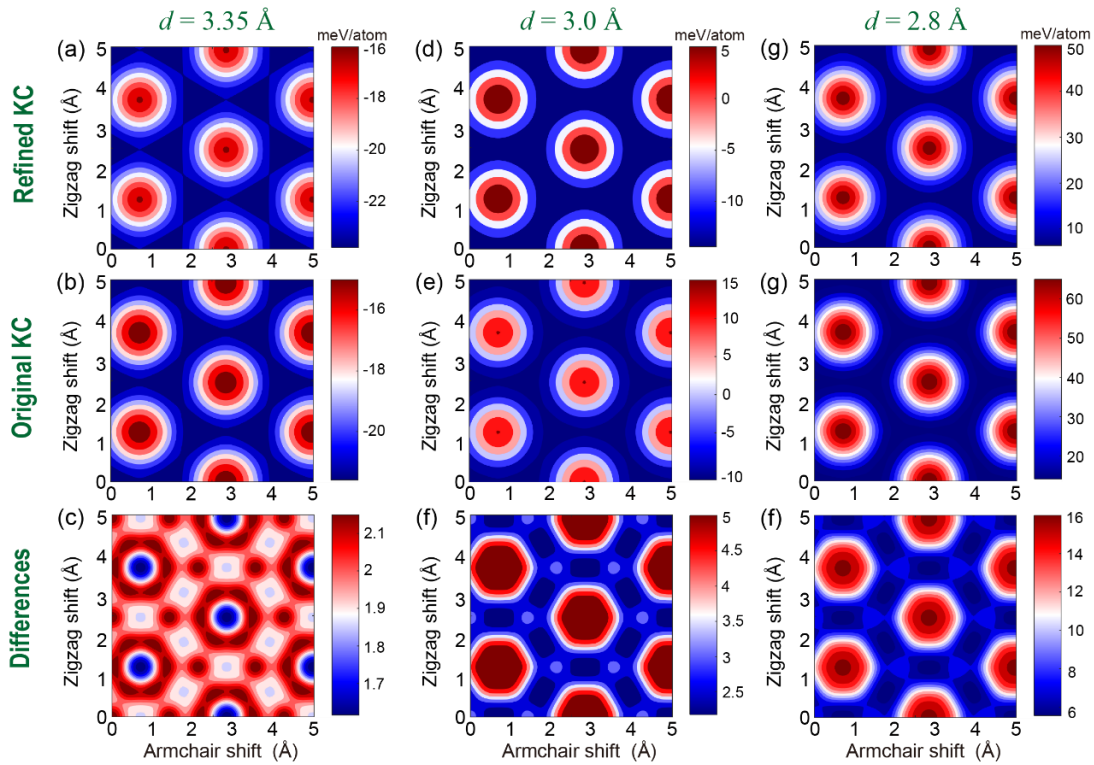


Figure S7. Sliding energy surfaces of periodic bilayer graphene for three different interlayer distances. The first and second rows present the sliding energy surfaces obtained at interlayer distances of 3.35 Å (left column), 3.0 Å (middle column), and 2.8 Å (right column) calculated using the refined [11](#) and original KC, [12](#) respectively. The third row presents the differences between the results obtained using the two KC parameterizations.

The first and second rows in **Figure S8** present the sliding energy surfaces of periodic bilayer *h*-BN with interlayer distances of 3.3 Å (left column), 3.0 Å (middle column), and 2.8 Å (right column) calculated using the refined and original ILP, respectively. The differences between the two are presented in the third row of the figure. Clearly, the differences between the sliding energy surfaces obtained using the two parameterizations increase in both magnitude and relative value as the interlayer distance decreases.

Specifically, the maximal absolute differences obtained are 0.49 (~4%), 1.8 (~10%), and 4.3 meV/atom (~40%), for interlayer distances of 3.3 Å, 3.0 Å, and 2.8 Å, respectively.

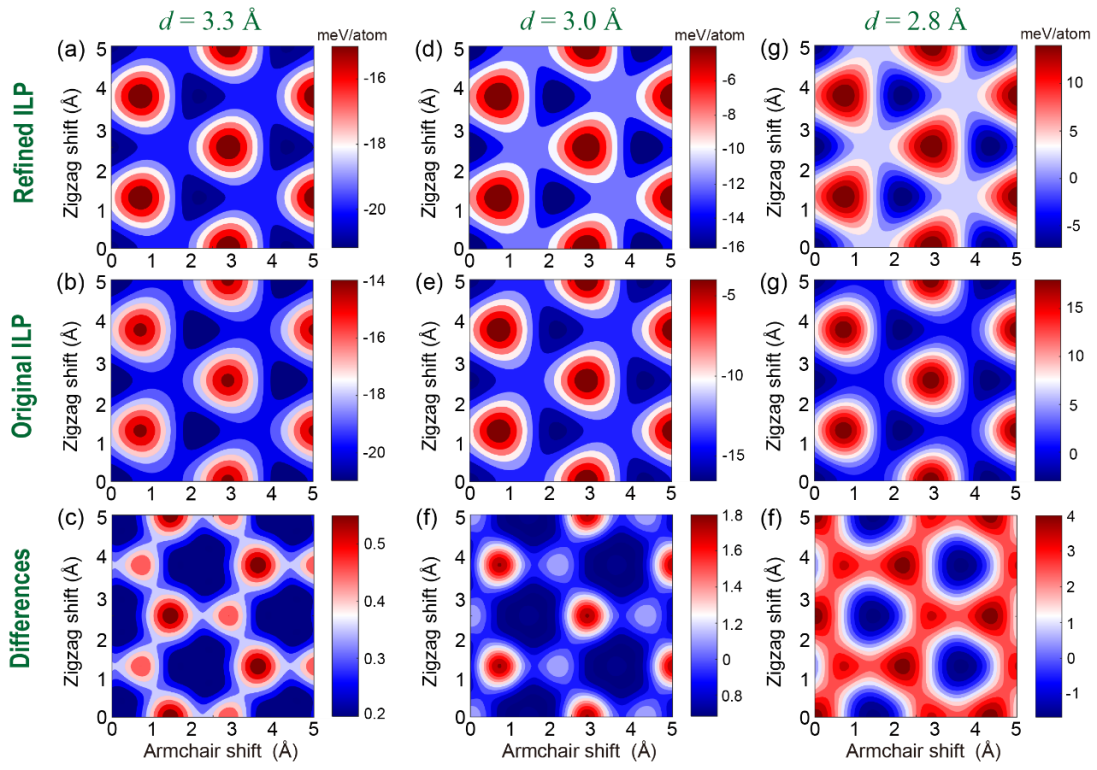


Figure S8. Sliding energy surfaces of periodic bilayer *h*-BN for three different interlayer distances. The first and second rows present the sliding energy surfaces obtained at interlayer distances of 3.3 Å (left column), 3.0 Å (middle column), and 2.8 Å (right column) calculated using the refined ¹¹ and original *h*-BN ILP,¹⁰ respectively. The third row presents the differences between the results obtained using the two ILP parameterizations.

5. Dispersive component of the sliding energy surfaces.

To evaluate the ability of the ILP to capture the dispersive component contribution to the sliding energy surface corrugation we plot in the second row of **Figure S9** the differences between the HSE + MBD results and the HSE only results (see first row of the figure) for the bulk graphite (left column), bulk *h*-BN (middle column), and alternating graphene/*h*-BN (left column) systems. Similar results for the TS dispersive component appear in the third row of the figure. Both the MBD and TS dispersive components are found to be typically lower than 2 meV/atom (apart from the TS component of the *h*-BN system that shows a corrugation of ~ 4 meV/atom), which is below the accuracy of the ILP fitting to the full HSE + MBD and HSE + TS reference data for these systems (see lower rows of Figures 2 and 3 of the main text). This indicates that the ILP cannot be expected to capture the dispersive component contribution to the sliding energy surface alone for the systems considered. We note in passing that, while the HSE contribution (first row of **Figure S9**) does not quantitatively capture the sliding energy surface, it is able to capture its overall symmetry obtained by the dispersion augmented methods.

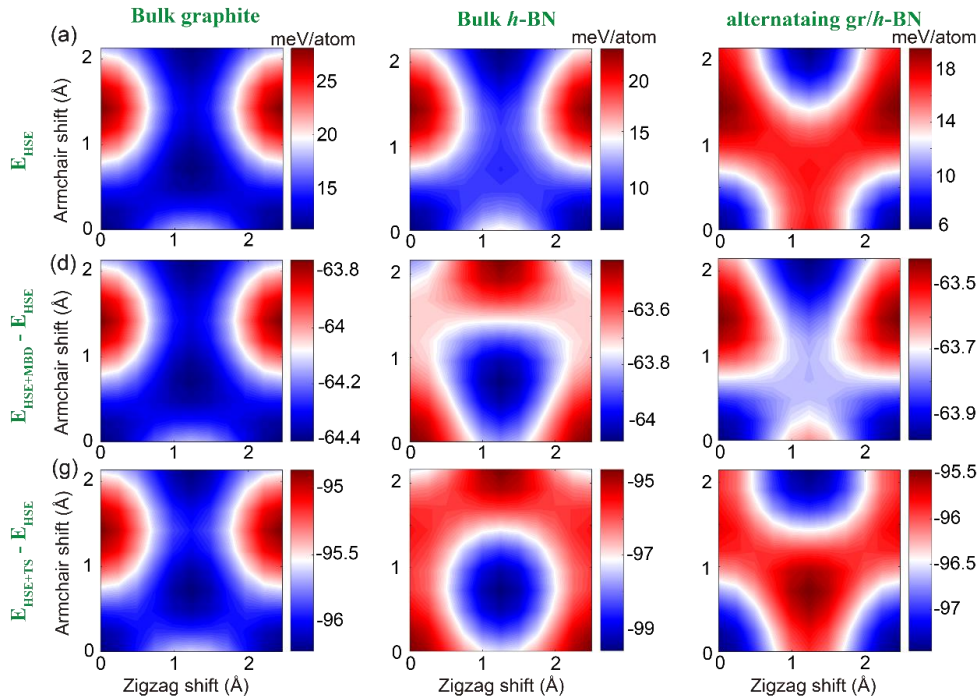


Figure S9. Dispersive component contribution to the sliding energy surfaces of the periodic structures considered, calculated at an interlayer distance of 3.3 Å. The first row presents the sliding energy surface of bulk graphite (left panels), bulk *h*-BN (middle panels), and an alternating graphene/*h*-BN stack (right panels) systems, calculated using HSE. The MBD and TS dispersion contributions to the sliding energy surfaces are presented in the second and third rows, respectively. These are obtained by subtracting the HSE surface from either the HSE + MBD or the HSE + TS results. The reported energies are measured relative to the value obtained for the infinitely separated layers and are normalized by the total number of atoms in the unit-cell.

6. Sliding energy barriers under different normal loads

To rationalize the differences in the friction forces obtained using the different ILP parameterizations (see Fig. 8 of the main text), we plot the energy barriers encountered during the sliding process as a function of the applied normal load for the four-layer graphene (**Figure S10a**) and *h*-BN (**Figure S10b**) model systems. For each stick-slip event, the energy barrier is evaluated from the ILP energy difference between the pre-slip and post-slip states. **Figure S10** presents the overall energy barrier, U_{sl} , obtained by averaging the results over several stick-slip events during steady-state sliding. The error bars represent the corresponding standard deviation resulting from thermal fluctuations. As can be seen, the friction force dependence on the normal load, presented in Figure 8 of the main text, follows the trends exhibited by the sliding energy barriers for the different ILP parameterizations.

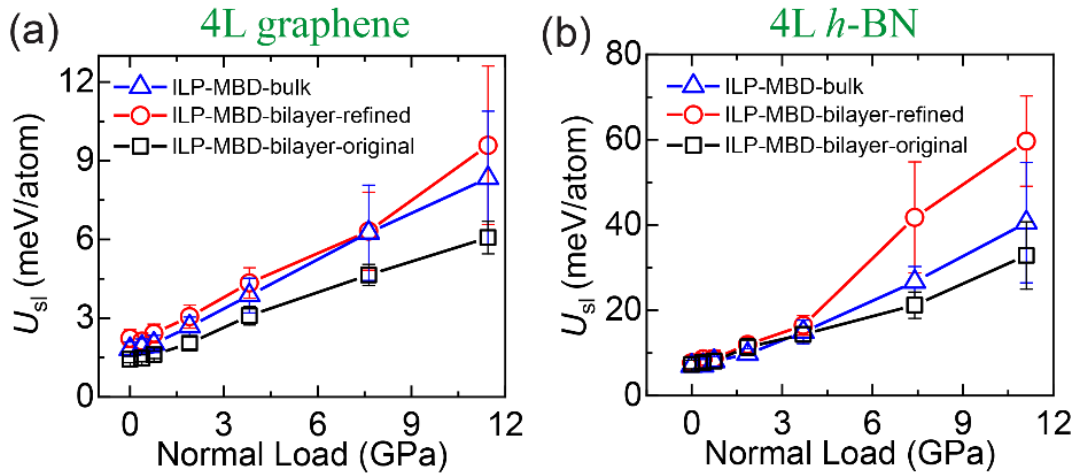


Figure S10. Normal load dependence of the sliding potential energy barriers obtained for model systems consisting of four layers of (a) graphene and (b) *h*-BN. The simulations are performed at a temperature of 300 K for three different ILP parameterizations as listed in the figure.

References

- (1) Heyd, J.; Scuseria, G. E.; Ernzerhof, M. Hybrid functionals based on a screened Coulomb potential. *J. Chem. Phys.* **2003**, *118*, 8207-8215.
- (2) Heyd, J.; Scuseria, G. E. Assessment and validation of a screened Coulomb hybrid density functional. *J. Chem. Phys.* **2004**, *120*, 7274-7280.
- (3) Heyd, J.; Scuseria, G. E. Efficient hybrid density functional calculations in solids: Assessment of the Heyd–Scuseria–Ernzerhof screened Coulomb hybrid functional. *J. Chem. Phys.* **2004**, *121*, 1187-1192.
- (4) Heyd, J.; Scuseria, G. E.; Ernzerhof, M. Erratum: “Hybrid functionals based on a screened Coulomb potential” [*J. Chem. Phys.* 118, 8207 (2003)]. **2006**, *124*, 219906.
- (5) Tkatchenko, A.; DiStasio, R. A.; Car, R.; Scheffler, M. Accurate and Efficient Method for Many-Body van der Waals Interactions. *Phys. Rev. Lett.* **2012**, *108*, 236402.
- (6) Ambrosetti, A.; Reilly, A. M.; DiStasio Jr., R. A.; Tkatchenko, A. Long-range correlation energy calculated from coupled atomic response functions. *J. Chem. Phys.* **2014**, *140*, 18A508.
- (7) Tkatchenko, A.; Scheffler, M. Accurate Molecular Van Der Waals Interactions from Ground-State Electron Density and Free-Atom Reference Data. *Phys. Rev. Lett.* **2009**, *102*, 073005.
- (8) Marom, N.; Tkatchenko, A.; Scheffler, M.; Kronik, L. Describing Both Dispersion Interactions and Electronic Structure Using Density Functional Theory: The Case of Metal–Phthalocyanine Dimers. *J. Chem. Theory Comput.* **2010**, *6*, 81-90.
- (9) Leven, I.; Maaravi, T.; Azuri, I.; Kronik, L.; Hod, O. Interlayer Potential for Graphene/h-BN Heterostructures. *J. Chem. Theory Comput.* **2016**, *12*, 2896-905.
- (10) Maaravi, T.; Leven, I.; Azuri, I.; Kronik, L.; Hod, O. Interlayer Potential for Homogeneous Graphene and Hexagonal Boron Nitride Systems: Reparametrization for Many-Body Dispersion Effects. *J. Phys. Chem. C* **2017**, *121*, 22826-22835.
- (11) Ouyang, W.; Mandelli, D.; Urbakh, M.; Hod, O. Nanoserpents: Graphene Nanoribbon Motion on Two-Dimensional Hexagonal Materials. *Nano Lett.* **2018**, *18*, 6009-6016.
- (12) Kolmogorov, A. N.; Crespi, V. H. Registry-dependent interlayer potential for graphitic systems. *Phys. Rev. B* **2005**, *71*, 235415.
- (13) Murnaghan, F. D. The Compressibility of Media under Extreme Pressures. *Proc. Natl. Acad. Sci.* **1944**, *30*, 244-247.
- (14) Birch, F. Finite Elastic Strain of Cubic Crystals. *Physical Review* **1947**, *71*, 809-824.
- (15) Birch, F. Elasticity and constitution of the Earth's interior. **1952**, *57*, 227-286.
- (16) Vinet, P.; Ferrante, J.; Smith, J. R.; Rose, J. H. A universal equation of state for solids. *Journal of Physics C: Solid State Physics* **1986**, *19*, L467-L473.
- (17) Vinet, P.; Smith, J. R.; Ferrante, J.; Rose, J. H. Temperature effects on the universal equation of state of solids. *Phys. Rev. B* **1987**, *35*, 1945-1953.
- (18) Ooi, N.; Rajan, V.; Gottlieb, J.; Catherine, Y.; Adams, J. B. Structural properties of hexagonal boron nitride. *Model. Simul. Mater. Sc* **2006**, *14*, 515.
- (19) Lynch, R. W.; Drickamer, H. G. Effect of High Pressure on the Lattice Parameters of Diamond, Graphite, and Hexagonal Boron Nitride. *J. Chem. Phys.* **1966**, *44*, 181-184.
- (20) Hanfland, M.; Beister, H.; Syassen, K. Graphite under pressure: Equation of state and first-order Raman modes. *Phys. Rev. B* **1989**, *39*, 12598-12603.
- (21) Zhao, Y. X.; Spain, I. L. X-ray diffraction data for graphite to 20 GPa. *Phys. Rev. B* **1989**, *40*, 993-997.
- (22) Solozhenko, V. L.; Will, G.; Elf, F. Isothermal compression of hexagonal graphite-like boron nitride up to 12 GPa. *Solid State Commun.* **1995**, *96*, 1-3.

(23) Zhao, Y.; Von Dreele, R. B.; Weidner, D. J.; Schiferl, D. P- V- T Data of hexagonal boron nitride h BN and determination of pressure and temperature using thermoelastic equations of state of multiple phases. *High Pressure Res.* **1997**, *15*, 369-386.

(24) Godec, Y. L.; Martinez-Garcia, D.; Mezouar, M.; Syfosse, G.; Itié, J. P.; Besson, J. M. Thermoelastic behaviour of hexagonal graphite-like boron nitride. *High Pressure Res.* **2000**, *17*, 35-46.